Formation and Maintenance of Shelfbreak Fronts in an Unstratified Flow*

GLEN GAWARKIEWICZ AND DAVID C. CHAPMAN

Woods Hole Oceanographic Institution, Woods Hole, Massachusetts

(Manuscript received 12 November 1990, in final form 4 March 1991)

ABSTRACT

A depth-averaged model with no density variations was used by Chapman to describe the formation of a passive tracer front at a shelfbreak. The relevance of this frontogenesis mechanism to cases that allow vertical variations is examined by considering the three-dimensional structure of a passive tracer front with explicit finite vertical mixing and bottom boundary layer dynamics. A three-dimensional primitive-equation numerical model is configured in a channel with a continental shelf, slope, and abyssal plain running the length of the channel. A vertically and horizontally uniform inflow is imposed over the shelf, with a large horizontal velocity shear near the shelfbreak. In the primitive-equation model, the offshore flow is concentrated in the bottom boundary layer while the alongshelf flow distribution is similar to the depth-averaged case; the presence of the bottom topography maintains a strong horizontal shear near the shelfbreak above the bottom boundary layer. This velocity shear causes a smooth passive tracer distribution imposed at the inflow boundary to develop strong cross-shelf gradients near the shelfbreak (i.e., a passive tracer front) within a rather short downstream distance, as in the depth-averaged model. Neutrally buoyant Lagrangian particles initialized above the bottom boundary layer are rapidly advected along the shelf with little cross-shelf motion. However, particles initialized within the bottom boundary layer move quickly offshore toward the shelfbreak and beyond while being advected alongshelf relatively slowly. The shelfbreak does *not* act as a barrier to the offshore transport of neutrally buoyant particles despite the presence of the passive tracer front. This results in a continuous net offshore transport from the shelf to the deep ocean due to the effects of bottom friction.

1. Introduction

Along the edge of many continental margins, a front separating shelf water from slope water is commonly observed to coincide with the sharp change in bottom slope at the shelfbreak. Examples include the Middle Atlantic Bight (Lyne and Csanady 1984), Georges Bank (Butman and Beardsley 1987), the eastern Bering Sea (Coachman 1986), and the Celtic Sea (Pingree et al. 1982). In each case, the continental shelf is fairly wide and the alongshelf mean flow is in the direction of propagation of free coastal-trapped waves. Perhaps the most distinguishing characteristic of shelfbreak fronts is their persistence in the presence of strong external forces, such as the surface wind stress and deep-ocean eddies. These forces can temporarily disrupt the fronts, but they reform rapidly after the forcing ceases.

Increasing attention has been devoted in recent years to the study of cross-shelf exchange of sediment, pollutants, and carbon in shelfbreak regions because of the potential for fronts to inhibit offshore transport (e.g., the Shelf Edge Exchange Processes observational program; Walsh et al. 1988). Furthermore, continental shelves are thought to play an important role in the global carbon cycle, and the exchange of carbon between shelves and the deep ocean has been recognized as a possibly significant aspect of climatic change (Walsh et al. 1981). Despite the indications of the important role of the shelfbreak front, a general understanding of the dynamics of the formation and maintenance of shelfbreak fronts is lacking at the present time.

There have been several attempts to describe the dynamics of shelfbreak frontal formation. One approach has been to examine the geostrophic adjustment of an initially prescribed, vertically uniform density field near shelfbreak topography and to show that the resultant velocity field is similar to that observed near shelfbreak fronts (Ou 1983; Hsueh and Cushman-Roisin 1983; Csanady 1984; Ou 1984; Wang 1984). All of these models are two dimensional, lacking alongshelf gradients of velocity and density. Consequently, they must conserve mass on the shelf and they each require the depth-averaged cross-shelf flow to be zero at every cross-shelf position. A weakness of some of these models is their neglect of bottom friction, which may be important dynamically over much of the shelf. The primary consequence of bottom friction is to produce a bottom frictional boundary layer with an associated cross-shelf transport. The result is a net offshore flow

---

* Woods Hole Oceanographic Institution Contribution Number 7595.

Corresponding author address: Dr. Glen Gawarkiewicz, Woods Hole Oceanographic Institution, Woods Hole, MA 02543.

when an alongshelf flow is oriented in the direction of the propagation of coastal-trapped waves and when externally imposed alongshelf pressure gradients are absent (e.g., Csanady 1978). Such mean alongshelf flows are commonly observed shoreward of the shelfbreak fronts, but these mean flows and their associated net offshore transport are omitted from the two-dimensional geostrophic adjustment models.

Other models have shown that the net offshore flow due to bottom friction can be significant. Wang (1982) has shown how bottom friction results in convergence of a shelf inflow at the shelfbreak, while Chapman et al. (1986) found that it was necessary, in a depth-averaged model of the Middle Atlantic Bight, to impose an onshore flow at the offshore boundary of the model domain in order to keep the shelf flow on the shelf. Without this inflow in the deep ocean, bottom friction steered the bulk of the shelf flow off the shelf and onto the slope over unrealistically short alongshelf distances.

Chapman (1986; hereafter C86) used a different approach from the geostrophic adjustment studies in order to include the mean alongshelf flow as well as the net offshore transport associated with bottom frictional effects. C86 assumed that density differences across the front were dynamically unimportant, because the temperature and salinity gradients at the shelfbreak front in the Middle Atlantic Bight have compensating contributions to the density field. At times, the thermohaline compensation is such that there are virtually no density gradients across the shelfbreak front, despite sharp gradients in both temperature and salinity fields. C86 then used a steady, depth-averaged model to study the alongshelf evolution of a *passive* tracer field. A fixed inflow was specified over part of the shelf at the upstream boundary (relative to the direction of free coastal-trapped wave propagation) and was allowed to adjust downstream. A passive tracer with a smooth cross-shelf distribution was then imposed at the upstream boundary and was advected and diffused through the velocity field. The model showed that large tracer gradients formed at the shelfbreak due to the velocity shear there and the rapid increase in depth seaward of the shelfbreak that quickly decreases the (depth-averaged) tracer concentrations.

Chapman's results show that the initial density gradient assumed in the geostrophic adjustment models is not necessary to generate a depth-averaged property front. However, while C86's model circumvents some limitations of previous models, it also includes a number of important simplifications, the consequences of which bear further investigation. For example, by depth-averaging the velocity and tracer fields, it is implicitly assumed that the model vertical eddy viscosity and diffusivity are infinite; so while the dynamical effects of bottom friction are present in a bulk sense, the bottom boundary layer is not explicitly resolved. Furthermore, the rapid decrease in tracer concentration beyond the shelfbreak could be merely an artifact of the depth averaging. A second obvious simplification is the lack of any density stratification which makes the shelfbreak front dynamically passive. Observed shelfbreak fronts usually have at least a weak density signal. Other simplifications include the assumption of steady laminar flow, which rules out the possibility of temporal variations and the growth of instabilities, and also the neglect of external forces such as wind stress and deep-ocean eddies that can disrupt the front as mentioned above.

Relaxing all of these constraints is not feasible for a single study, so we examine here the three-dimensional nature of the passive tracer front proposed by C86. In particular, we repeat the calculations done with the depth-averaged model but now using a three-dimensional primitive-equation model (linearized for the present study) in which the bottom boundary layer is explicitly resolved and finite vertical viscosity and diffusivity are included. The most important simplification in the model is the neglect of stratification, which is expected to be of some importance in the shelfbreak region. We do this in order to gain physical insight into the dynamics of the passive tracer front and as a prerequisite for understanding the more complicated case with stratification, which is the subject of an ongoing study. Before launching into the three-dimensional calculations, we extend some of the depth-averaged results of C86 in order to review the previous results and more completely describe the behavior of the depth-averaged system (section 2). Then the three-dimensional model and the numerical procedure are described (section 3), followed by a direct comparison between the depth-averaged model and the three-dimensional model results (section 4). Next, some Lagrangian properties of the flow are described (section 5), and this leads to an examination of the role of the deep ocean circulation that Chapman et al. (1986) found to be so important in the depth-averaged model (section 6). Finally, a summary appears in section 7.

2. The depth-averaged model

To facilitate comparison with the three-dimensional model, it is useful to examine briefly the sensitivity of the depth-averaged model to horizontal diffusivity and bottom friction. The steady, linear, depth-averaged momentum and continuity equations are

$$-f\bar{v} = -g\zeta_x - \frac{r\bar{u}}{h} \qquad (1)$$

$$f\bar{u} = -g\zeta_y - \frac{r\bar{v}}{h} \qquad (2)$$

$$h\bar{u}_x + (h\bar{v})_y = 0 \qquad (3)$$

where $\bar{u}$ and $\bar{v}$ are the depth-averaged velocities in the alongshelf (x) and cross-shelf (y) directions, ζ the sea surface elevation, r the linear bottom friction coefficient, f the Coriolis parameter (fixed at 10^{-4} s^{-1} throughout), g the gravitational acceleration, and h the bottom depth, which varies only in the cross-shelf direction. Subscripts denote partial differentiation. For simplicity, we assume that r is constant whereas C86 allowed r to vary with depth. Also, our coordinate system is rotated by 90° from C86. The bottom topography used throughout consists of a gently sloping shelf and a steep slope bordering a flat bottom abyssal plain (Fig. 1). To avoid numerical difficulties, the bottom slope is made continuous by adding quadratic terms near the shelfbreak and where the slope meets the abyssal plain:

$$h(y) = \begin{cases} 50.0 + 2y \quad \text{for} \quad y < 50 \text{ km} \\ 160.0 + 1.5(y - 50 \text{ km})^2 - 0.1\,(y - 60 \text{ km})^2 \\ \qquad \qquad \text{for} \quad 50 \text{ km} < y < 60 \text{ km} \\ 310.0 + 30.0(y - 60 \text{ km}) \\ \qquad \qquad \text{for} \quad 60 \text{ km} < y < 100 \text{ km} \\ 1660.0 - 1.5(y - 110 \text{ km})^2 \\ \qquad \qquad \text{for} \quad 100 \text{ km} < y < 110 \text{ km} \\ 1660.0 \quad \text{for} \quad y > 110 \text{ km} \end{cases}$$

where h is in units of meters and y is in units of kilometers [see Fig. 3b for a plot of $h(y)$]. The abyssal plain is chosen to be fairly shallow (1660 m) compared to the real ocean in order to allow vertical resolution of flow structures with a reasonably small number of vertical modes in the three-dimensional model (see section 3). Most of the important flow features occur in water shallower than 400 m, so we are confident that the relatively shallow abyssal plain has little effect on the present results. The depth-averaged model domain is 200 km by 200 km with a grid spacing of 3.125 km in both x and y directions.

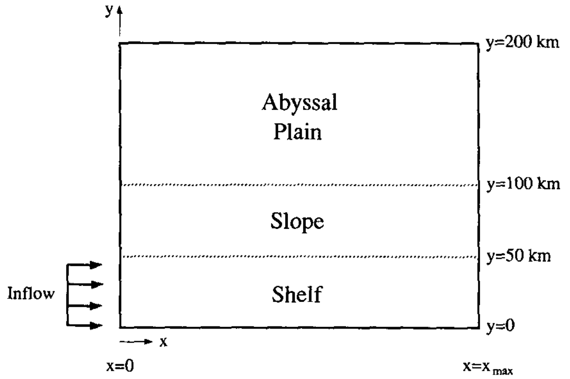

FIG. 1. A plan view of the configuration of both the depth-averaged and three-dimensional models. The coast is at the bottom ($y = 0$). The topography includes a shelf with a bottom slope of 0.002, a slope with a bottom slope of 0.03, and a flat abyssal plain with a depth of 1660 m. The channel length is 200 km ($x_{\max}$) for the depth-averaged model and 400 km for the three-dimensional model. The channel width is 200 km in all cases. A vertically uniform inflow is imposed at the upstream boundary ($x = 0$) and allowed to evolve downstream.

The solution procedure is identical to that of C86. For a prescribed inflow at the upstream boundary (relative to the direction of coastal-trapped wave propagation) the velocity field is found by introducing a transport streamfunction ($\Psi_x = -h\bar{v}$, $\Psi_y = h\bar{u}$) into (1)–(3) and solving numerically using the method of Fiadeiro and Veronis (1977) with a smoothness condition of $\Psi_{xx} = -h\bar{v}_x = 0$ at the downstream boundary ($x = 200$ km). Having found the steady flow field, a passive tracer is introduced at the upstream boundary and is advected and diffused through the model domain. The conservative advection–diffusion equation describing the depth-averaged tracer concentration $\bar{\epsilon}$ is

$$\frac{1}{h}(\bar{u}\bar{\epsilon}_x + \bar{v}\bar{\epsilon}_y) = K\left(\bar{\epsilon}_{xx} + \frac{h_y}{h}\bar{\epsilon}_y + \bar{\epsilon}_{yy}\right) \tag{4}$$

where K is the (constant) horizontal eddy diffusivity. A no-flux condition is applied at the coast, $\bar{\epsilon}_y = 0$ at $y = 0$, while the tracer concentration vanishes at the offshore boundary, $\bar{\epsilon} = 0$ at $y = 200$ km. A smoothness condition of $\bar{\epsilon}_{xx} = 0$ is imposed at the downstream boundary ($x = 200$ km). After specifying the topography h and the Coriolis parameter f, the resulting flow and tracer distribution depend on the choice of the bottom friction coefficient r, the horizontal diffusivity K, the inflow velocity magnitude and distribution, and the tracer concentration at the upstream boundary.

For our basic or standard case, an initial inflow of $\bar{u} = 0.10$ m s^{-1} is imposed over the shelf ($y < 50$ km) with no flow seaward of the shelf ($\bar{u} = 0$ for $y > 50$ km). The horizontal diffusivity is $K = 100$ m^2 s^{-1} and the bottom friction coefficient is $r = 5 \times 10^{-4}$ m s^{-1}. The passive tracer distribution at the upstream boundary is $\bar{\epsilon} = \cos(\pi y / 2L_w)$, where $L_w = 200$ km is the width of the channel. This choice satisfies (4) and the boundary conditions on $\bar{\epsilon}$ when there is no inflow; i.e., $\bar{u} = \bar{v} = 0$, and no topography, i.e., $h_y = 0$. The resulting transport streamfunction for this case is shown in Fig. 2a. While the bulk of the flow remains on the shelf, there is a small offshore component to the flow that distributes the flow seaward as the flow evolves in the alongshelf direction, in the manner of the arrested topographic wave (Csanady 1978). The corresponding tracer field (Fig. 2b) has become homogenized over the shelf and in the abyssal plain, leaving large cross-shelf gradients primarily near the shelfbreak. As C86 has shown, these gradients result from advection as well as the additional diffusion of tracer induced by the bottom slope [the middle term on the right-hand side of (4)].

The importance of advection can be illustrated by considering the effect of diffusion alone over the bottom topography. If $\bar{u} = \bar{v} = 0$, then (4) becomes

(a) Transport Streamfunction

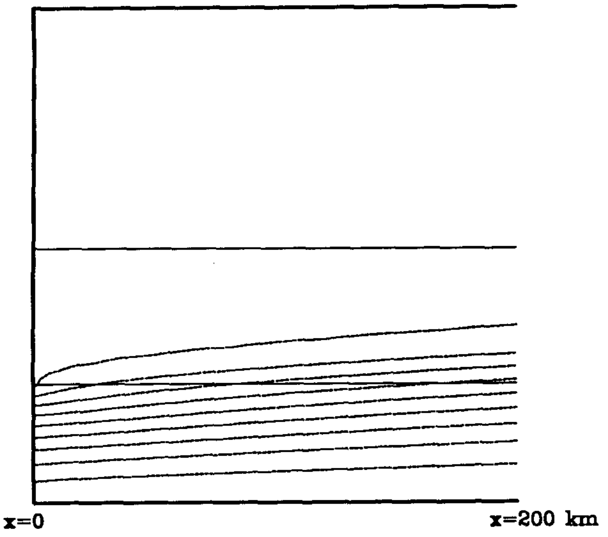

(b) Tracer Concentration

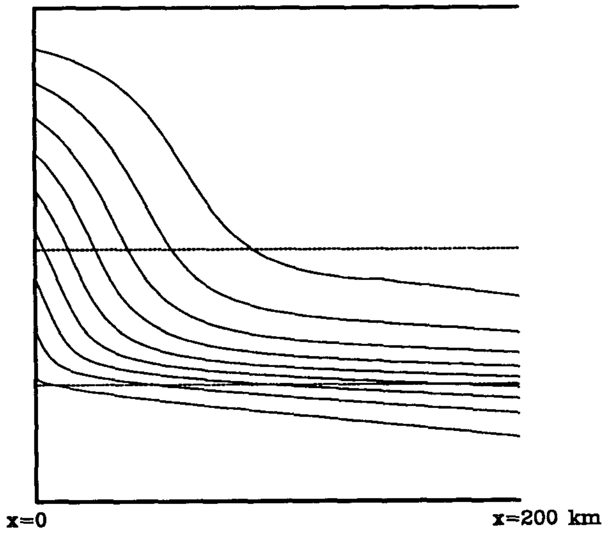

FIG. 2. Plan views of the (a) depth-averaged transport streamfunction and (b) depth-averaged tracer concentration for the standard case of a 0.10 m s^{-1} uniform inflow imposed over the shelf ($y \leqslant 50$ km) with $K = 100$ m^2 s^{-1} and $r = 5 \times 10^{-4}$ m s^{-1}. The contour interval for the streamfunction is 5×10^4 m^3 s^{-1}; the streamfunction value is 0 at the coastal boundary while the value at the most seaward contour is -4.5×10^5 m^3 s^{-1}. The contour interval for the tracer concentration is 0.1, and the values range from 0.9 at the most shoreward contour to 0.1 at the most seaward contour. The shelfbreak at $y = 50$ km is denoted by the lower horizontal line, while the upper horizontal line marks the 1650 m isobath near the shoreward edge of the abyssal plain. The domain size is 200 km by 200 km.

$$\bar{\epsilon}_{xx} + \frac{h_y}{h}\bar{\epsilon}_y + \bar{\epsilon}_{yy} = 0. \qquad (5)$$

The lowest-mode eigenfunction satisfying (5) and the boundary conditions on $\bar{\epsilon}$ are shown by the solid curve in Fig. 3a. For comparison, the dashed curve is the imposed upstream tracer distribution which, as mentioned above, is the solution of (5) with no topography (i.e., $h_y = 0$). The dash–dot curve is the cross-shelf tracer distribution at $x = 150$ km from Fig. 2b, which includes the effects of advection. The presence of bottom topography alters the tracer distribution slightly, but the effects of advection clearly dominate the downstream tracer distribution.

The effect of varying the bottom friction coefficient by two orders of magnitude (from 5×10^{-5} to 5×10^{-3} m s^{-1}) is shown in Fig. 4, in which the alongshelf and cross-shelf velocities and tracer concentration at $x = 150$ km are plotted as a function of offshore distance. (The upstream condition is also shown for comparison.) As expected, the larger values of the bottom friction coefficient lead to greater cross-shelf flow in the bottom boundary layer, thus forcing the flow to cross the isobaths more readily with a corresponding decrease in the maximum alongshelf velocity (Fig. 4a). Consequently, as r increases, the alongshelf velocity distribution reaches farther offshore and the maximum gradient ($\bar{u}_y$) decreases. Obviously, the offshore component of the flow must increase with increasing r, but in each case, the cross-shelf maximum in $\bar{v}$ occurs just shoreward of the shelfbreak (Fig. 4b). The large differences in the velocity field have little effect on the passive tracer distribution (Fig. 4c) because the tracer gradients depend primarily on the length scale of the horizontal shear in the alongshelf velocity, $\bar{u}_y$, rather than the velocity magnitude. The maximum cross-shelf

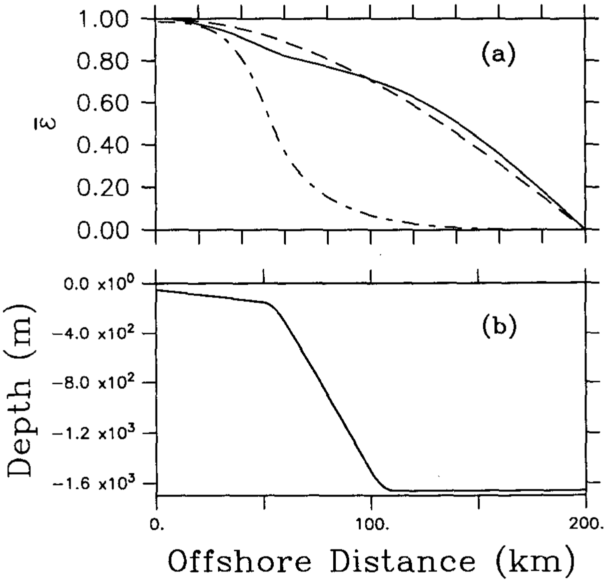

FIG. 3. (a) The cross-shelf variation of tracer concentration $\bar{\epsilon}$: (dashed curve) at the upstream boundary, (dash–dot curve) at $x = 150$ km for the standard case of Fig. 2, and (solid curve) for the lowest-mode eigenfunction of the purely diffusive case given by (5). (b) The standard bottom topography.

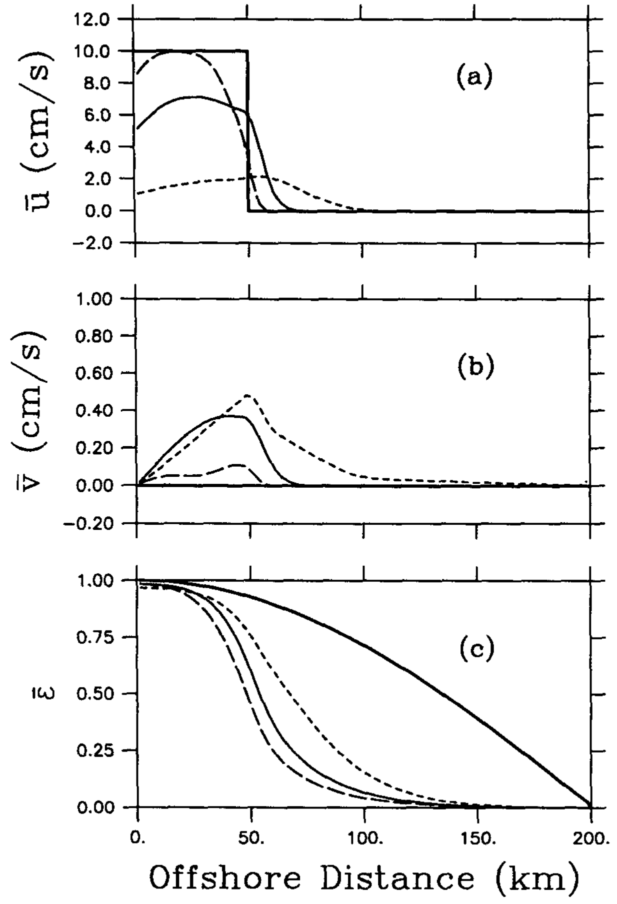

FIG. 4. The cross-shelf variation (at x = 150 km) of (a) alongshelf velocity $\bar{u}$, (b) cross-shelf velocity $\bar{v}$, and (c) tracer concentration $\bar{\epsilon}$ for three different values of the linear bottom friction coefficient in the depth-averaged model. The curves are for $r = 5 \times 10^{-3}$ m s^{-1} (short dash), 5×10^{-4} m s^{-1} (solid), and 5×10^{-5} m s^{-1} (long dash). Other parameters are the same as in Fig. 2. The thick solid curves in each panel represent the values at the upstream boundary.

gradient of the tracer ($\bar{\epsilon}_y$) remains fairly constant, although increasing r tends to displace the tracer front seaward. Thus, bottom friction is important in determining the structure of the velocity field but has little effect on the strength of the tracer front, tending only to displace the front slightly.

The horizontal diffusivity K appears only in the tracer equation (4) and thus does not affect the velocity field. Furthermore, the linearity of the momentum equations makes the velocities directly proportional to the inflow velocity. Therefore, because the tracer dynamics are simply a balance between advection and diffusion, decreasing the diffusivity has the same qualitative effect as increasing the upstream inflow velocity, and that is an increase in the maximum tracer gradient (Fig. 5).

It is important to note that there is a great deal of uncertainty in the choice of horizontal diffusivity based on observations. Garvine et al. (1989) estimated values of K at the shelfbreak south of New England that were not statistically different from zero, while Garrett et al. (1985) estimated K by following iceberg trajectories on the Labrador shelf and obtained a value of 1200 m^2 s^{-1}. Thus, there is no clear choice for an appropriate value of K for numerical studies. On the other hand, the observed mean alongshelf velocity (represented here as the shelf inflow velocity) is relatively well known being on the order of 5 to 10 cm s^{-1} for most shelfbreak front regions. Therefore, the tracer distribution in the depth-averaged model is fairly insensitive to such a small range in the inflow velocity but is quite sensitive to the large range of possible K values, so the horizontal diffusivity becomes the more important parameter.

It is clear, from Fig. 4 and C86, that the location of the tracer front coincides with the location of the maximum horizontal shear in the alongshelf velocity, $\bar{u}_y$. This is also a well-known result from meteorology, i.e., that a deformation field leads to frontogenesis (e.g., Pedlosky 1979, Chapter 8). In the present case, however, the topography acts to maintain the shear near the shelfbreak. If the inflow is restricted to any portion of the shelf (such that the shear at the upstream boundary is shoreward of the shelfbreak), the flow will move offshore until it reaches the shelfbreak where the sudden change in bottom slope greatly reduces the offshore spreading. Once the velocity shear maximum reaches the shelfbreak, it is maintained there for large alongshelf distances due to the bottom topography (for example, see Fig. 3a of C86). Thus, a large horizontal shear develops near the shelfbreak and is maintained there regardless of the details of the inflow distribution, provided that all of the inflow is shoreward of the shelfbreak. In this way the bottom topography can play a crucial role in setting the location of the maximum horizontal shear in the alongshelf velocity which, in

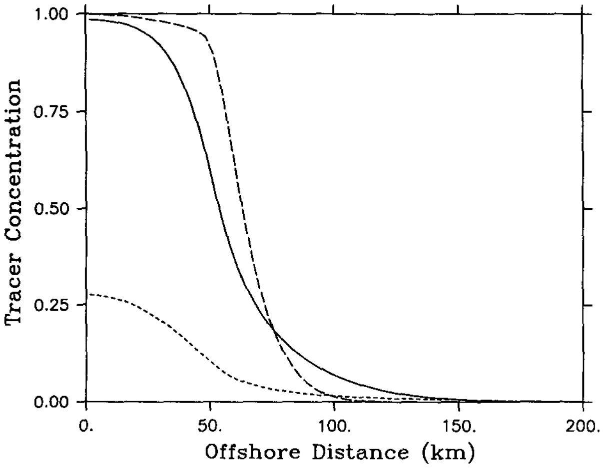

FIG. 5. The cross-shelf variation in the tracer concentration (x = 150 km) for K = 1000 m^2 s^{-1} (short dash), 100 m^2 s^{-1} (solid), and 10 m^2 s^{-1} (long dash) in the depth-averaged model. Other parameters are the same as in Fig. 2.

turn, defines the location of the tracer front. For typical alongshelf flows over the continental shelf, this location is near the shelfbreak.

On the other hand, if the inflow extends seaward of the shelfbreak with a large shear over the slope, the maximum passive tracer gradient coincides with the shear. The steep bottom slope causes only weak offshore spreading of the inflow, so the horizontal shear remains near the location imposed at the upstream boundary. If no shear is present at the upstream boundary, e.g., a horizontally uniform inflow, no passive tracer front forms at all.

3. The three-dimensional model

In order to test the robustness of the results obtained from the depth-averaged model, we use the three-dimensional primitive-equation model described in detail by Haidvogel et al. (1991), in which the vertical structure is explicitly resolved. The model uses finite differences in the horizontal and a spectral expansion in the vertical with modified Chebyshev polynomials as basis functions. A sigma (topography-following) coordinate system is used in the vertical to allow for arbitrary bottom topography. The model solves the fully nonlinear, hydrostatic equations, but for the present study nonlinear advection of momentum is omitted, so the momentum and continuity equations used here are

$$u_t - fv = -\frac{1}{\rho} p_x + A_V u_{zz} + F_u \qquad (6)$$

$$v_t + fu = -\frac{1}{\rho} p_y + A_V v_{zz} + F_v \qquad (7)$$

$$0 = -p_z - \rho g \qquad (8)$$

$$u_x + v_y + w_z = 0 \qquad (9)$$

where u and v are the alongshelf (x) and cross-shelf (y) velocities, p is the pressure, ρ is the (constant) density, t is time, and z is the vertical coordinate, which is positive upward; A_V is the (constant) vertical eddy viscosity. The functions F_u and F_v represent Laplacian momentum mixing terms needed for numerical stability and are applied along sigma-coordinate surfaces with an effective eddy viscosity of 100 $\text{m}^2\,\text{s}^{-1}$. Subscripts x, y, z, and t denote partial differentiation. The three-dimensional passive tracer concentration ϵ is described by

$$\epsilon_t + u\epsilon_x + v\epsilon_y + w\epsilon_z = K_V \epsilon_{zz} + F_\epsilon \qquad (10)$$

where K_V is the (constant) vertical eddy diffusivity, and F_ϵ is another Laplacian mixing term like F_u and F_v and is given an effective eddy diffusivity of 100 $\text{m}^2\,\text{s}^{-1}$.

At the surface, the vertical shear stress is set to zero for u and v, so that

$$A_V u_z = A_V v_z = 0 \quad \text{at} \quad z = 0. \qquad (11)$$

At the bottom, the velocity shear is proportional to the velocity:

$$A_V u_z = -ru \quad \text{at} \quad z = -h \qquad (12)$$

$$A_V v_z = -rv \quad \text{at} \quad z = -h \qquad (13)$$

where r is the bottom friction coefficient. Thus the bottom Ekman layer is resolved, but the log layer beneath is not. Free-slip conditions are used for the velocities at both the offshore and coastal boundaries. The flux of tracer through the surface, bottom, and channel walls is set to zero. At the upstream boundary ($x = 0$), the horizontal velocities and the tracer concentration are prescribed.

The downstream boundary is more complicated because it is an open boundary through which the flow should pass unimpeded and with no reflection of energy. No perfect open boundary condition exists for our situation, so we have devised a condition that makes use of the present model formulation as follows. In the primitive-equation model, the interior flow field is computed in two parts. The vertically averaged momentum equations are combined to form a vorticity equation which is time-stepped directly. The depth-averaged velocity field is recovered by solving an elliptic equation for the barotropic streamfunction. Then the vertically varying part of the solution is time-stepped separately before being combined with the depth-averaged velocities to obtain the complete solution. [See Haidvogel et al. (1991) for the details.]. At the downstream open boundary, a similar approach is used. An Orlanski (1976) radiation condition is applied to the depth-averaged vorticity to obtain an estimate on the open boundary. Then, with the additional assumption that $\partial^2(\text{barotropic streamfunction})/\partial x^2 = 0$ at the boundary, the barotropic streamfunction (and hence the depth-averaged part of u) can be easily found from a tridiagonal matrix equation. (Remember that the barotropic streamfunction is prescribed at the offshore wall based on the upstream inflow.) A similar Orlanski (1976) radiation condition is then applied to the vertically varying part of the velocity field to obtain an estimate at the boundary, which is added to the depth-averaged part to obtain the entire velocity field at the open boundary. The cross-shelf velocity is computed directly from an Orlanski (1976) radiation condition. For the tracer concentration, the boundary value is set equal to the closest interior value when $u > 0$ and is unchanged when $u < 0$.

This open boundary condition works quite well for the present set of problems because of the simplified dynamics. The initial adjustment at $t = 0$ produces only continental shelf waves, which propagate in the $+x$ direction. Internal gravity waves do not exist because the fluid is unstratified, and the rigid lid has filtered out the surface gravity waves. Upon reaching the downstream boundary, the continental shelf waves can reflect, but only as very short continental shelf waves.

These short waves are either unresolved spatially or they are rapidly damped by the stabilizing horizontal mixing (F_u and F_v), so they do not travel far upstream. The possibility of barotropic and baroclinic Kelvin waves trapped at the offshore boundary is lost since the lid is rigid and ρ is constant.

Tests using channels of various lengths confirm that this treatment of the open boundary has little influence on the interior solution. Nevertheless, in order to prevent any effects of the open boundary from appearing in the region of interest for comparison with the depth-averaged model ($0 < x < 200$ km), we have used a channel with an alongshelf length of 400 km and a width of 200 km for all of the three-dimensional model results presented here. Only the velocity and tracer fields for $x \leqslant 200$ km will be described. The grid contains 129 points in the alongshelf (x) direction and 49 points in the cross-shelf (y) direction, giving a uniform grid spacing of 3.125 km in the x direction and 4.17 km in the y direction. The time step is 432 s throughout, or 0.005 day.

Seven Chebyshev polynomials are used in the vertical after tests with a larger number of modes gave nearly identical results. The collocation points, or equivalent grid points in the vertical, correspond to the extrema of the Chebyshev polynomials, and are concentrated near the surface and bottom boundaries, which greatly improves the resolution of the boundary layers. It should be noted that the spectral representation is more efficient than standard grid points in the sense that seven vertical modes are equivalent to a greater number of standard grid points because of the additional information contained in the polynomials between the collocation points.

The model is run for 30 days of simulation time which is short enough to be economical and long enough to exceed the spindown and advective time scales for the first 200 km of the model domain. The results presented are nearly unchanged when the model is run for longer times.

4. Comparison of depth-averaged and three-dimensional results

To compare the three-dimensional model results with the results from the standard case of the depth-averaged model of section 2, the common parameters should be identical. Therefore, in the standard three-dimensional case, a vertically uniform inflow of $u = 0.10$ m s^{-1} is specified at the upstream boundary for $y < 50$ km. The bottom topography is the same as in section 2. The upstream tracer concentration is vertically uniform with $\epsilon = \cos(\pi y/2L_w)$ where $L_w = 200$ km, and the bottom friction coefficient is $r = 5 \times 10^{-4}$ m s^{-1}.

The only important difference between the depth-averaged model and the three-dimensional model is the resolution of vertical structure in the latter. In particular, the vertical diffusion of momentum is not assumed to be infinite, which means that the bottom boundary layer is explicitly resolved. In other words, the role of the vertical viscosity is primarily to set the vertical scale over which the stress due to bottom friction is distributed, i.e., the Ekman layer thickness $(2A_V/f)^{1/2}$. In the depth-averaged model, an implicitly infinite viscosity distributes the stress throughout the entire water column. A more realistic value which we choose for the standard three-dimensional case, $A_V = 2 \times 10^{-3}$ m^2 s^{-1}, yields a boundary layer thickness of 6.3 m. Similarly, vertical diffusion of the tracer is not assumed infinite, so that the tracer distribution need not remain vertically uniform as in the depth-averaged model. Again we choose a value of $K_V = 2 \times 10^{-3}$ m^2 s^{-1} for the standard three-dimensional case. It is the effect of this difference in vertical structure on the velocity and tracer fields that we examine next. The important questions are whether or not the velocity shear found near the shelfbreak in the depth-averaged model still exists in the three-dimensional model and whether or not a sharp tracer front will still form at the shelfbreak in the presence of finite vertical diffusion.

In the depth-averaged case, the offshore velocity of the bottom boundary layer is distributed over the entire water column, so the flow is steered only slightly seaward of the isobaths (Fig. 2a) and, of course, does not vary with depth. As expected, the barotropic transport streamfunction (i.e., depth-averaged velocity) for the three-dimensional model (Fig. 6a) is nearly identical to that of the depth-averaged model (Fig. 2a). (This essentially confirms that the vertical structure is the only difference between the two models.) However, the horizontal velocities vary strongly with depth near the bottom. The surface velocities (Fig. 6b) are nearly parallel to the isobaths with almost no offshore component, while the velocities at the bottom (Fig. 6c) are directed almost 45° offshore due to the flow in the bottom boundary layer. The offshore flow is concentrated in the bottom boundary layer, and the alongshelf flow is nearly vertically uniform above the bottom boundary layer.

A cross-shelf slice of the alongshelf velocity at $x = 150$ km from the three-dimensional model is shown in Fig. 7a while the corresponding slice for the depth-averaged model appears in Fig. 7b. Note that only half of the channel width ($y \leqslant 100$ km) and only the upper 400 m of the water column are shown. The rapid deceleration of the flow seaward of the shelfbreak is present in both models; however, the alongshelf velocity decreases rapidly near the bottom in the three-dimensional model. The maximum velocity at the surface in the three-dimensional model is 0.096 m s^{-1} at $y = 21$ km, while the maximum velocity in the depth-averaged model is 0.071 m s^{-1} at $y = 25$ km. This difference exists because the bottom boundary layer slows the alongshelf velocity only near the bottom in the three-dimensional model, whereas the decrease is spread

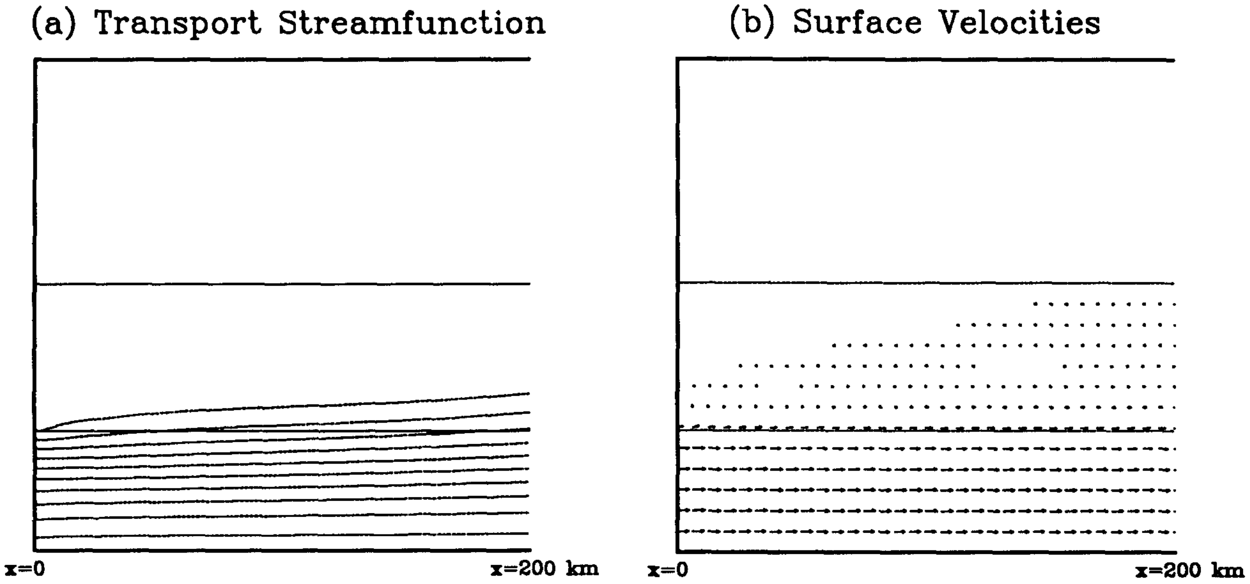

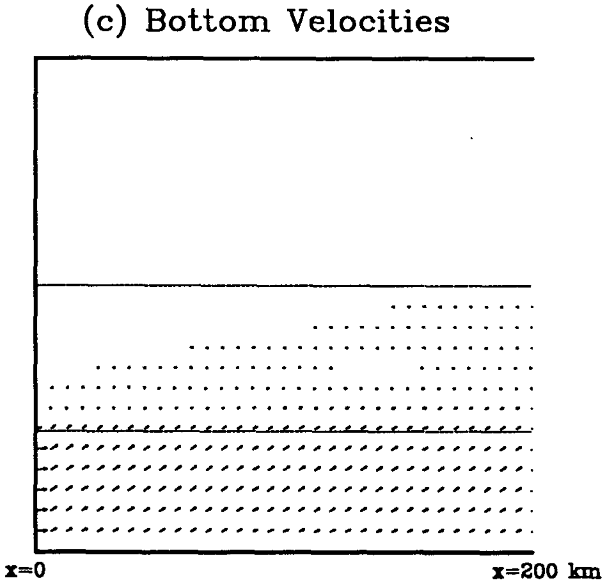

FIG. 6. Plan views from the standard three-dimensional model case. (a) Barotropic (depth-averaged) transport streamfunction. The contour interval is 5×10^4 m^3 s^{-1}; the streamfunction value is 0 at the coastal boundary while the value at the most seaward contour is -5×10^5 m^3 s^{-1}. (b) Velocity vectors at the surface (shown at every second grid point). (c) Velocity vectors at the bottom ($z = -h$). The maximum vector length in (b) and (c) is 0.10 m s^{-1}. The model domain in each case is 200 km by 200 km.

throughout the water column in the depth-averaged model. The effect is more pronounced in shallower water.

The offshore velocity shear of the alongshelf flow (u_y) at the surface in the three-dimensional model is concentrated at the shelfbreak as it is in the depth-averaged case (Fig. 8). However, at $x = 150$ km, the maximum velocity shear magnitude at the surface of the three-dimensional model is 3.65×10^{-6} s^{-1} and occurs 2 km seaward of the shelfbreak, while the maximum velocity shear magnitude for the depth-averaged case is 5.33×10^{-6} s^{-1} and occurs 6 km seaward of the shelfbreak. The smaller maximum velocity shear magnitude in the three-dimensional model is due to the presence of the dissipation term (F_u) in the alongshelf momentum equation (6). In the base case (Fig. 8), the value of the Laplacian mixing coefficient along sigma surfaces is 100 m^2 s^{-1}. As the mixing coefficient for the Laplacian mixing is decreased to 50 and 25 m^2 s^{-1}, the maximum shear magnitude increases to 4.34 and 5.02 ($\times 10^{-6}$ s^{-1}), respectively. Below 25 m^2 s^{-1}, the maximum shear magnitude behaves erratically, and it is likely that spurious computational modes are present. Thus the structure of the shear is comparable in

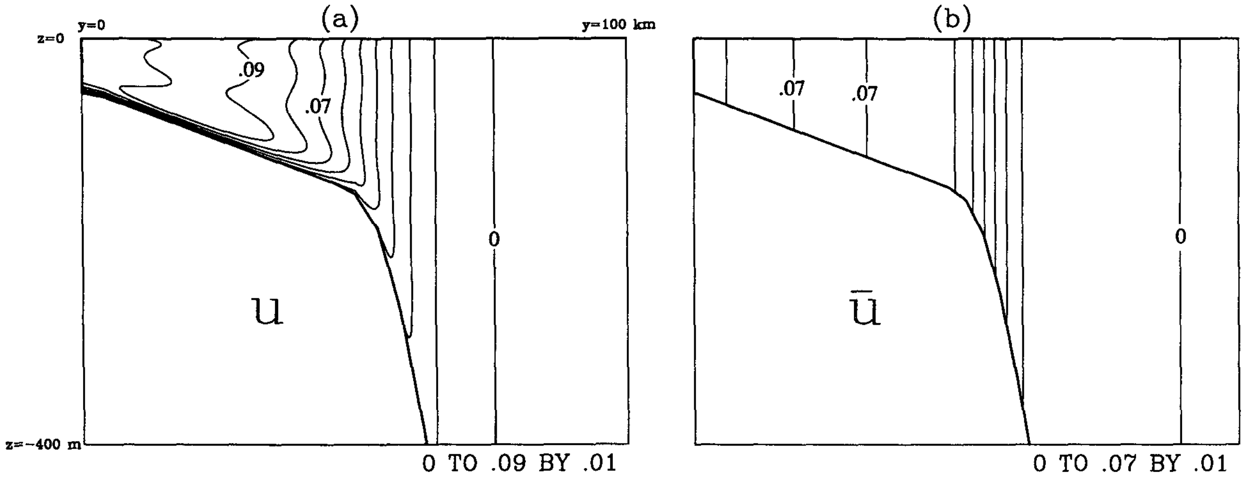

FIG. 7. A cross-shelf section at $x = 150$ km of the alongshelf velocity in (a) the three-dimensional model (u) and in (b) the depth-averaged model ($\bar{u}$). The contour interval in each is 0.01 m s^{-1} with the most seaward contour being 0.0 m s^{-1}. Both panels show only the results from the coast to $y = 100$ km offshore and the upper 400 m of the water column.

the two models, and the maximum shear magnitudes become nearly equal when the Laplacian mixing coefficient is reduced.

On the other hand, the cross-shelf velocity structure is considerably different between the two models (Fig. 9). In the three-dimensional case (Fig. 9a), the bottom Ekman layer has a thickness of $(2A_V/f)^{1/2} = 6.3$ m, and the cross-shelf velocity is concentrated in this region, with a maximum cross-shelf velocity of 0.031 m s^{-1} at $y = 33$ km. The cross-shelf velocity in the depth-averaged case (Fig. 9b) is an order of magnitude smaller than in the three-dimensional case, ranging from 0.002 to 0.0025 m s^{-1} for 30 km $< y <$ 50 km and decreasing rapidly to zero seaward of the shelfbreak. The presence of the bottom boundary layer leads to a complicated three-dimensional pattern in the Lagrangrian description of the flow, as will be seen in section 5.

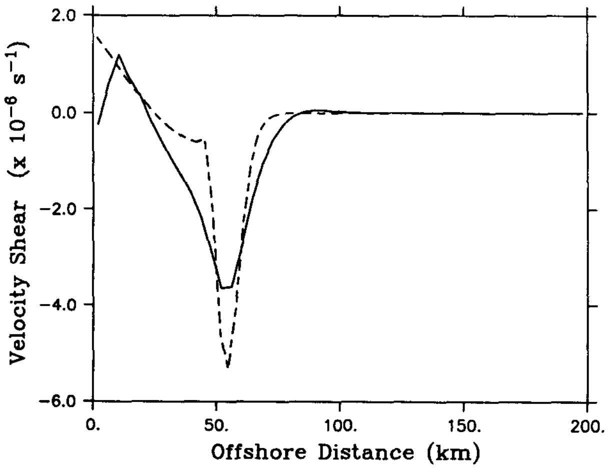

FIG. 8. The cross-shelf variation at $x = 150$ km in the horizontal shear of the alongshelf velocity at the surface in the standard three-dimensional model (u_y, solid) and in the depth-averaged model ($\bar{u}_y$, dashed).

The three-dimensional velocity structure has a profound effect on the distribution of the cross-shelf transport at the shelfbreak. The depth-integrated cross-shelf transport at $y = 50$ km (e.g., the shelfbreak) as a function of the alongshelf distance x is shown in Fig. 10 (solid line) in comparison with the cross-shelf transport in the bottom 6.7 m of the water column (dashed line). Within the first 20 km downstream of the specified inflow, a large portion of the cross-shelf transport past the shelfbreak occurs above the bottom boundary layer as the velocity discontinuity introduced at the offshore edge of the initial inflow adjusts rapidly. This adjustment occurs due to both Laplacian mixing [F_u in (6)] and divergences in Ekman pumping rates from the bottom boundary layer into the nearly geostrophic interior. As the flow progresses downstream, the cross-shelf transport in the bottom boundary layer (i.e., one Ekman layer thickness) becomes an increasingly larger fraction of the depth-integrated cross-shelf transport, reaching greater than half of the total at $x = 169$ km, despite occupying a small portion of the 150 m water column at the shelfbreak.

The differences in the velocity fields do not appreciably change the tracer distribution (Fig. 11). The surface distribution of the tracer for the three-dimensional case is very similar to that of the depth-averaged case (Fig. 2b). In both models the sharpest cross-shelf gradients are located near the shelfbreak, and the maximum values of tracer concentration decrease downshelf. The major differences occur over the abyssal plain

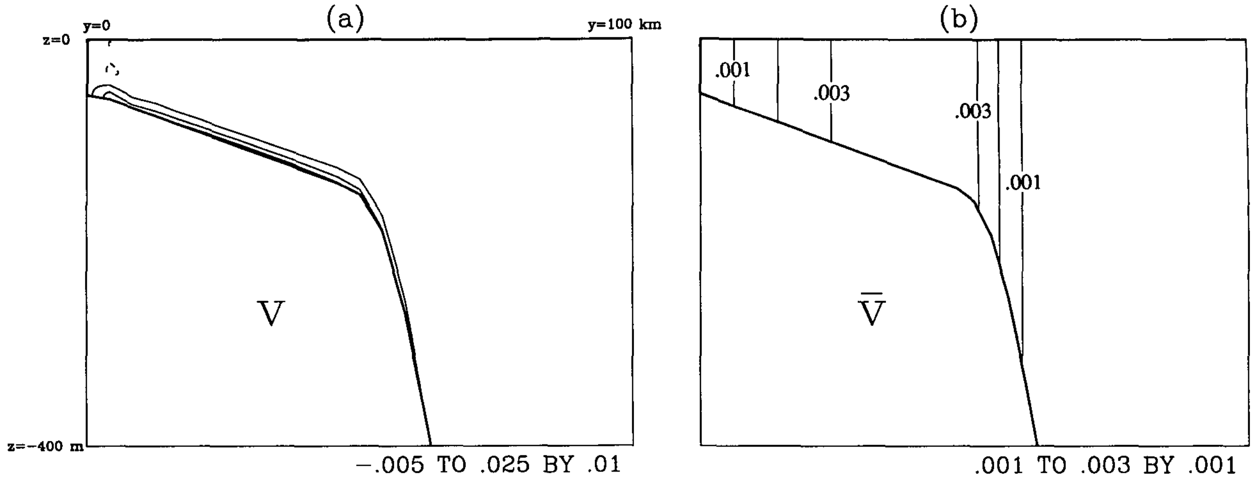

FIG. 9. A cross-shelf section at x = 150 km of cross-shelf velocity in (a) the standard three-dimensional model (v) and in (b) the depth-averaged model ($\bar{v}$). The contour interval in (a) is 0.01 m s^{-1} and the values vary from −0.005 m s^{-1} to a maximum of 0.03 m s^{-1} near the bottom at the edge of the shelf. The contour interval in (b) is 0.001 m s^{-1}, and the maximum is 0.003 m s^{-1} at midshelf. Both panels show only the results from the coast to y = 100 km offshore and the upper 400 m of the water column.

where the three-dimensional model has not truly reached a steady state because of the long time scale associated with the almost purely diffusive processes acting in the deep water.

As with the horizontal mixing coefficient, there is considerable uncertainty in the appropriate value for the vertical mixing coefficients A_V and K_V. Estimates made over the outer shelf in the Middle Atlantic Bight are on the order of 0.001 to 0.005 m^2 s^{-1} (Garrett and Horne 1978). Therefore, we examine next the tracer distribution for various choices of A_V and K_V (Fig. 12). The depth-averaged tracer distribution (Fig. 12a) has effectively infinite vertical mixing coefficients, $A_V = K_V = \infty$. For a large but finite value of $A_V = K_V$ = 0.005 m^2 s^{-1} (Fig. 12b), distribution of the tracer is still nearly vertically uniform, and the bottom boundary layer has not substantially altered the tracer distribution compared to the depth-averaged case. For our standard case of $A_V = K_V$ = 0.002 m^2 s^{-1}, the tracer distribution shows only a slight vertical variation (Fig. 12c). When A_V and K_V are reduced to 0.0005 m^2 s^{-1} (Fig. 12d),

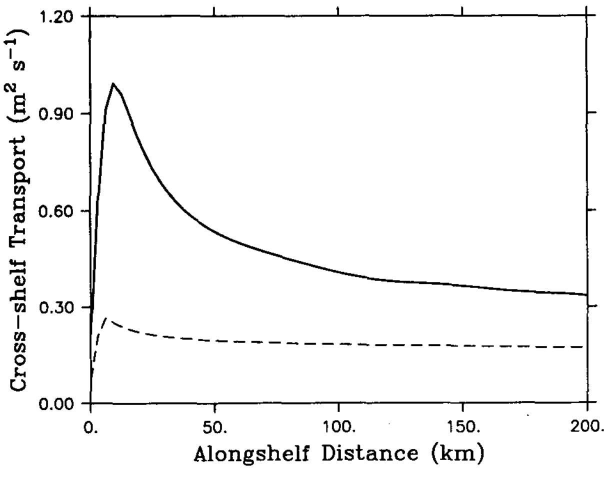

FIG. 10. The cross-shelf transport at the shelfbreak (y = 50 km) for the standard three-dimensional model as a function of alongshelf distance x for the entire water column (solid) and the bottom 6.7 m (dashed).

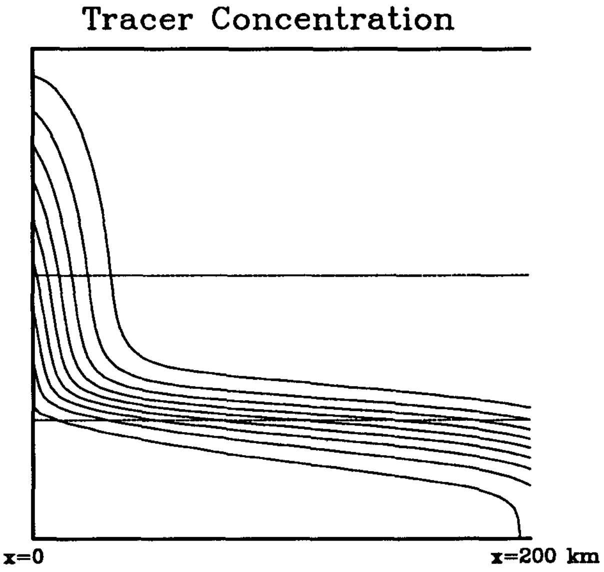

FIG. 11. A plan view of the tracer concentration ϵ at the surface in the standard three-dimensional model. The contour interval is 0.1 and the values range from 0.9 at the most shoreward contour to 0.1 at the most seaward contour. The domain is 200 km by 200 km.

the thickness of the bottom boundary layer decreases to 3.4 m and the vertical gradients of the tracer distribution become apparent. The decreasing vertical structure with increasing vertical diffusivity is consistent with the implicitly assumed infinite vertical diffusivity of the depth-averaged model. However, even a fairly small value of K_V and A_V, with the bottom boundary layer thickness a small fraction of the water column, is still large enough to smooth the tracer field across the relatively weak vertical shear at the top of the bottom boundary layer; the result being a nearly vertically uniform tracer distribution.

The momentum balances for the three-dimensional model are quite simple. For the alongshelf momentum equation (6), the flow is nearly geostrophic above the bottom boundary layer, but the terms are small compared with those in the bottom boundary layer where a classical Ekman balance exists between the vertical diffusion of the alongshelf velocity, $A_V u_{zz}$, and the Coriolis force, $-fv$. For the cross-shelf momentum equation (7), the balance is again almost geostrophic above the bottom boundary layer, with the cross-shelf pressure gradient, $-\rho^{-1}p_y$, nearly balancing the Coriolis force, fu; while in the bottom boundary layer the pressure gradient is nearly balanced by the vertical diffusion of the cross-shelf velocity.

5. Lagrangian flow description

The three-dimensional flow field can also be further illuminated by following neutrally buoyant Lagrangian particles through the computational model domain. Particle paths are computed using a second-order Runge-Kutta scheme with bilinear interpolation between the velocities at the four nearest grid points. A detailed description of the technique is provided by Hedstrom (1990). For the results shown here, the velocity field was held fixed as if it were steady while the particles moved through it. Comparisons with particles being advected through the evolving flow showed no significant differences.

In a depth-averaged flow, particles simply follow streamlines, and no explicit account of depth changes is possible. However, as described in section 4, the resolution of the bottom boundary layer in the three-dimensional model leads to a cross-shelf flow which is concentrated near the bottom. Therefore, particles lo-

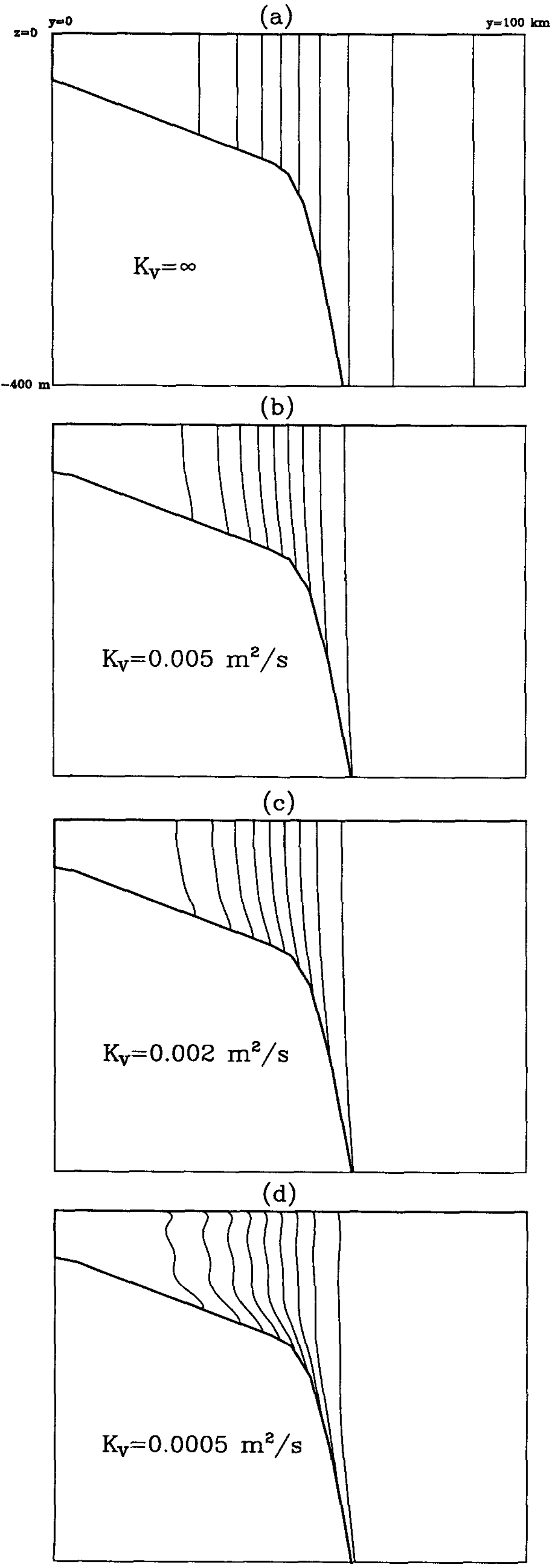

FIG. 12. Cross-shelf sections of the tracer concentrations at $x = 150$ km for (a) the standard case of the depth-averaged model, (b) the three-dimensional model with $K_V = A_V = 0.005$ m^2 s^{-1}, (c) the three-dimensional model with $K_V = A_V = 0.002$ m^2 s^{-1}, and (d) the three-dimensional model with $K_V = A_V = 0.0005$ m^2 s^{-1}. All panels show only the results from the coast to $y = 100$ km offshore and the upper 400 m of the water column. The contour interval in each case is 0.1 with the most shoreward contour equal to 0.9 and the most seaward equal to 0.1.

cated near the bottom exhibit substantially different behavior from particles located in the upper part of the water column as seen in Fig. 13, which shows plan views of particle trajectories initialized at depths of 10 m below the surface and 5 m above the bottom. (The flow field is that of the standard case for the three-dimensional model shown in Fig. 6 with a bottom Ekman layer thickness of 6.3 m.) The particles that begin near the surface (solid curves) are advected alongshelf rapidly at 0.08 to 0.09 m s^{-1} and exhibit little offshore motion. By comparison, the particles initialized 5 m above the bottom (dashed curves) exhibit a strong offshore flow of 0.01–0.02 m s^{-1} shoreward of the shelfbreak and are advected alongshelf at a slower velocity. As particles cross the shelfbreak (at $y = 50$ km), the alongshelf flow diminishes rapidly, which in turn slows the offshelf flow of near-bottom particles in the bottom boundary layer. The convergence near the shelfbreak is much less pronounced for the near-surface particles because they must travel a much longer alongshelf distance before they reach the shelfbreak.

The trajectories of the near-surface particles are representative of the entire water column above the bottom boundary layer as illustrated by a projection of several particle paths onto the cross-shelf and vertical plane (Fig. 14). The particles initialized above the bottom boundary layer undergo almost no cross-shelf or vertical motion. However, those within the bottom boundary layer move rapidly offshore, and, in addition, remain in the bottom boundary layer over the continental slope making a vertical excursion of as much as 200 m in 30 days.

Most importantly, the horizontal shear at the shelfbreak does not act as a barrier to the neutrally buoyant particles near the bottom. As the flow progresses alongshelf, the seaward edge of the alongshelf flow continually moves farther offshore, down the slope. The bottom boundary layer then extends offshore beyond the shelfbreak, and the near-bottom particles continue beyond the shelfbreak in the bottom boundary layer flow. This may appear paradoxical because the passive tracer front is established and persists near the shelfbreak, but the dynamics of the particles and the passive tracer are different. The particles are simply advected through the flow, while the passive tracer is advected and diffused through the flow. The dominant diffusive term for the passive tracer is the vertical diffusion term, $K_v \epsilon_{zz}$, which in the standard case ($K_v = 0.002$ m^2 s^{-1}) was large enough to nearly homogenize the tracer in the vertical and maintain the cross-shelf tracer gradients at the shelfbreak. Smaller values of the vertical diffusivity would lead to more qualitative similarity between the behavior of the passive tracer and the particles, with larger tracer concentrations extending seaward of the shelfbreak near the bottom as suggested by Fig. 12d (although in that case the vertical eddy viscosity, A_v, was also reduced).

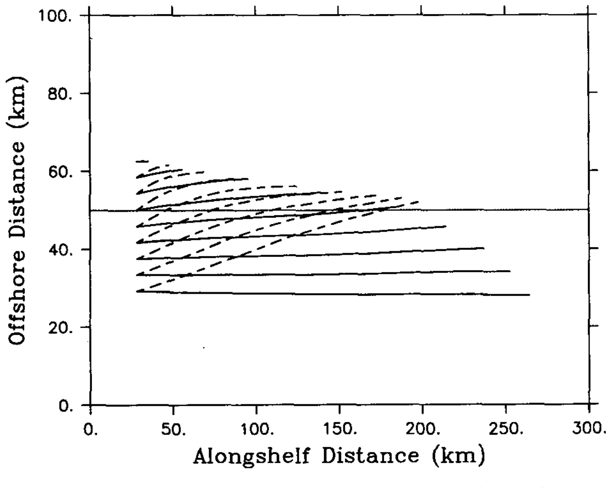

FIG. 13. A plan view of the trajectories of ten particles initialized 10 m below the surface (solid) and ten particles initialized 5 m above the bottom (dashed) at $x = 33$ km in the standard three-dimensional model. The shelfbreak at $y = 50$ km is marked by a thin, dashed horizontal line. Only half of the cross-shelf domain ($0 < y < 100$ km) is shown. Each curve represents a 30 day trajectory.

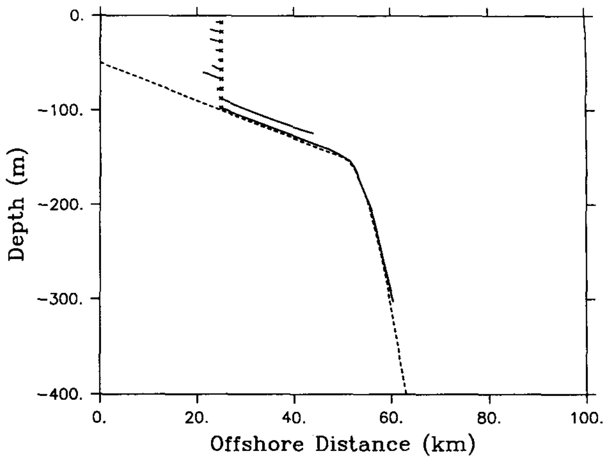

FIG. 14. A cross-shelf (y–z) projection of the paths of ten particles initialized at $x = 33$ km and $y = 30$ km, and evenly spaced in the vertical in the standard three-dimensional model. Each curve represents a 30 day trajectory.

6. Deep-ocean inflow

The primary goal of this study has been to determine whether or not the tracer front mechanism demonstrated in the depth-averaged model also occurs in the three-dimensional model. If the addition of vertical structure and finite vertical diffusion substantially changed the nature of the tracer front, or prevented the formation of a tracer front, then the mechanism described by C86 would, at best, have questionable relevance to actual shelfbreak fronts. The results of section 4 showed that the tracer distribution obtained using the three-dimensional model with a vertical diffusivity in the range of estimated ocean values, i.e., 0.001 to 0.005 $m^2 s^{-1}$, was nearly identical to the tracer distribution found in the depth-averaged model. Thus the mechanism proposed by C86 for the formation of passive tracer fronts appears to carry over to three-dimensional flows.

One difficulty with the three-dimensional model, however, is that the shelf flow leaks offshore (seaward of the shelfbreak) relatively rapidly. This was also a problem in the depth-averaged model of the Gulf of Maine and Middle Atlantic Bight described by Chapman et al. (1986). The shelf flow turned offshore over relatively short distances and a significant portion of the shelf inflow did not reach the southern end of the Middle Atlantic Bight, where much of the actual shelf flow is believed to leave the shelf. Chapman et al. (1986) found that by introducing an additional deep-ocean inflow (either at the upstream boundary or through the offshore boundary, crudely representing the observed slope circulation) the offshore flow of shelf water was substantially reduced. It was concluded that the role of the deep-ocean and slope circulation is to oppose the frictionally induced off-shelf flow and thereby inhibit the shelf water from moving seaward of the shelfbreak.

It is interesting to examine whether or not such a deep-ocean inflow can reduce the offshore flow present in the three-dimensional model. Therefore, we have repeated the standard three-dimensional model run, but with a uniform 0.10 m s^{-1} inflow over the entire upstream boundary. Figure 15 shows the proportion of shelf inflow that remains on the shelf (shelf transport at each x divided by shelf inflow) for both this case and the standard case when the inflow is restricted to $y < 50$ km. More than 90% of the shelf inflow is still on the shelf after traveling 200 km downstream when the deep inflow is included, whereas only about 77% of the shelf inflow is still on the shelf at $x = 200$ km for the standard case. This result is consistent with the depth-averaged results discussed by Chapman et al. (1986) and seems to support their conclusion about the deep-ocean influence. However, the details of the three-dimensional flow reveal a different behavior and lead to a different conclusion. Near-surface particle trajectories for 30 days are shown in Fig. 16 for the two cases. The particles travel considerably farther alongshelf when the deep-ocean inflow is included, and the near-surface flow is nearly parallel to the coast. In fact, the deep-ocean inflow results in higher velocities throughout the channel with the added effect that the offshore transport in the bottom boundary layer is correspondingly larger as well. As a result, particles initialized near the bottom travel much farther alongshelf *and* offshore when the deep-ocean inflow is included than they do with the limited inflow of the standard case (Fig. 17). There is a region of horizontal convergence seaward of the shelfbreak in the standard case, but with the deep-ocean inflow, the velocity is larger over the entire slope region and the particles continue to move rapidly offshore.

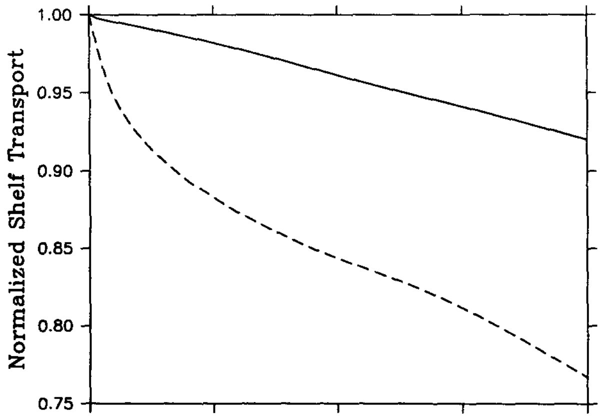

FIG. 15. The proportion of shelf inflow that remains on the shelf (shelf transport at each x divided by the shelf inflow at the upstream boundary), as a function of the alongshelf distance x in the three-dimensional model. The solid line is obtained for the case of a uniform inflow velocity of 0.10 m s^{-1} along the entire upstream boundary ($0 \leqslant y \leqslant 200$ km). The dashed line is obtained for the standard case with an inflow velocity of 0.10 m s^{-1} limited to the shelf ($y \leqslant 50$ km).

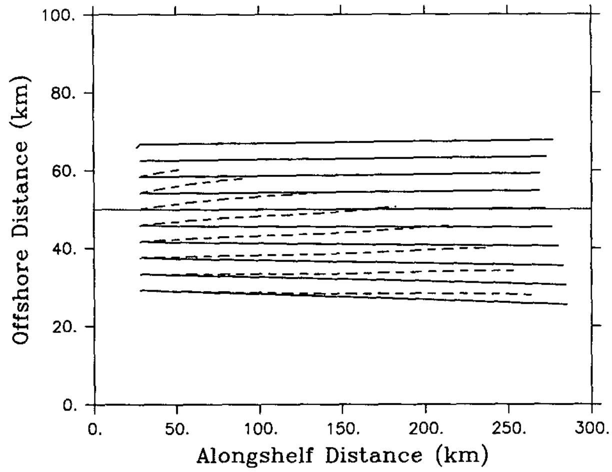

FIG. 16. A plan view of the trajectories of near-surface particles (released at 10 m depth) with a uniform inflow of 0.10 m s^{-1} across the entire channel (solid) and a uniform inflow of 0.10 m s^{-1} limited to the shelf (dashed). Each curve represents a 30 day trajectory. The shelfbreak at $y = 50$ km is marked by a thin horizontal line.

These results indicate that the depth-averaged model, in some sense, has been misleading. Even though a greater percentage of the inflow on the shelf remains on the shelf when a deep-ocean inflow is present, the bottom boundary layer actually ejects particles farther and faster offshore, so that the leakage near the bottom

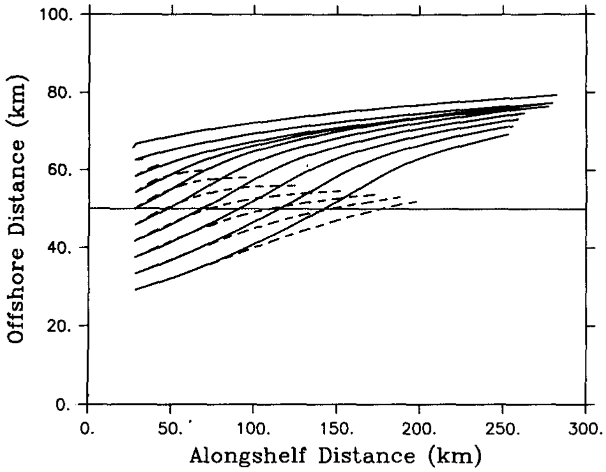

FIG. 17. A plan view of the trajectories of near bottom particles (released 5 m above the bottom) with a uniform inflow of 0.10 m s^{-1} across the entire channel (solid) and a uniform inflow of 0.10 m s^{-1} limited to the shelf (dashed). Each curve represents a 30 day trajectory. The shelfbreak at $y = 50$ km is marked by a thin horizontal line.

at the shelfbreak is more pronounced. Chapman et al. (1986) used the depth-averaged results alone, in which the flow appears to remain on the shelf for greater distances alongshelf, and concluded that the exchange with the deep ocean must be reduced. However, the depth averaging actually obscures the dramatic offshore flow in the bottom boundary layer, which would most likely dominate the cross-shelf transport of particles in the absence of wind or eddy forcing. Paradoxically, in the three-dimensional model a deep-ocean inflow actually acts to *enhance* the offshore motion in the bottom boundary layer and leads to a conclusion opposite that of Chapman et al. (1986). The deep-ocean inflow inhibits offshore motion in the upper, geostrophic portion of the water column, but actually increases the offshore flow in the bottom boundary layer.

7. Summary

We have examined the three-dimensional structure of the shelfbreak tracer front formation mechanism proposed by C86 by comparing his depth-averaged results to those from a three-dimensional primitive-equation numerical model. An alongshelf inflow is imposed over the continental shelf and allowed to adjust under the influence of rotation and bottom friction. Then a smoothly distributed passive tracer is introduced at the upstream boundary and is advected and diffused through the flow field. In the depth-averaged case, the flow is primarily alongshelf with a gradual offshore transport due to the effects of bottom friction. A strong shear develops near the shelfbreak due to the change in bottom slope there, and this leads to large cross-shelf gradients in the tracer field near the shelfbreak. C86 suggested that this may represent a mechanism for the formation and maintenance of the shelfbreak front.

The three-dimensional velocity structure is more complicated. The offshore flow is concentrated in the bottom (Ekman) boundary layer, which the depth-averaged model does not resolve. Above the bottom boundary layer, the flow is nearly alongshelf and geostrophic. A strong cross-shelf shear still develops near the shelfbreak and large cross-shelf tracer gradients also form there. Therefore, the tracer front formation mechanism of the depth-averaged model is still active in three dimensions.

However, the concentration of the offshore flow in the bottom boundary layer has some important consequences. In particular, neutrally buoyant particles in the bottom boundary layer behave far differently than those in the upper portion of the water column; they travel rapidly offshore and may move well beyond the shelfbreak, sinking by hundreds of meters. This means that neither the shelfbreak nor the tracer front acts as a barrier to particles in the bottom boundary layer, even in cases where the alongshelf velocity (and therefore the cross-shelf velocity) decreases rapidly seaward of the shelfbreak. Particles in the upper portion of the water column also drift seaward but with a much slower velocity, and due to the large alongshelf velocities, they are carried much farther alongshelf before crossing the shelfbreak. Such a flow has important implications for the fate of particles that might be advected vertically through the water column by high frequency processes such as internal waves or turbulence. Particles that somehow rise out of the bottom boundary layer would be transported at a much greater velocity alongshelf and would move offshore very slowly. Particles which might sink into the bottom boundary layer would slow in the alongshelf direction, but would start to move offshore rapidly.

The present results show that a deep-ocean inflow, which appears to reduce this offshore flow by keeping more of the depth-averaged flow on the shelf, actually leads to *increased* offshore flow in the bottom boundary layer. In fact, all unstratified flows over the continental shelf that move in the direction of coastal-trapped wave propagation and include bottom friction are inherently three dimensional in this way and will generate a strong offshore flow in the bottom boundary layer; so the shelf flow will gradually leak offshore while moving alongshelf. Thus two-dimensional models that conserve mass on the shelf and lack alongshelf gradients cannot consider the dynamical role of bottom friction in driving mean offshore flows. Such two-dimensional models must either implicitly assume the presence of some unspecified dynamics, such as an offshore pressure gradient to oppose the net offshore flow, or explicitly assume that the leakage is slow.

The present model indicates that the shelfbreak (tracer) front in an unstratified flow is very leaky near the bottom. However, this result appears to be at odds with the limited available observations, which suggest that suspended particular matter remains along isopycnals that detach from the bottom near the shelfbreak (Churchill et al. 1988), while larger particles with significant settling velocities penetrate the front and are carried to significant depths over the slope near the bottom (Biscaye et al. 1988). Thus, the absence of density stratification represents an important limitation on the applicability of the present results because it ensures the continuity of the bottom boundary layer between the shelf and slope and eliminates any possibility of the bottom boundary layer detaching and following isopycnals. We suspect that stratification is the one model feature which, when added, may change the present results qualitatively. Other generalizations, such as more complex forms of vertical mixing and diffusion or more realistic treatments of bottom friction, will probably not appreciably alter the present results. We speculate that the basic frontal formation mechanism shown here will also form a front when stratification is included, but that the leakiness near the bottom will be greatly reduced because the particles will be inclined to follow the isopycnals near the shelfbreak. Such an investigation is now underway.

Acknowledgments. We are grateful for the efforts of Dale Haidvogel, Kate Hedstrom, and Aike Beckmann who developed model improvements and provided technical assistance during the course of this research. Discussions with Steve Lentz were quite helpful. Comments from Ken Brink and an anonymous reviewer improved the clarity of the manuscript. Financial support was provided by the National Science Foundation under Grant OCE88-16015. Computer facilities at the National Center for Atmospheric Research in Boulder, Colorado, were used for the numerical calculations. NCAR is funded by the National Science Foundation.

REFERENCES

Biscaye, P. E., R. F. Anderson and B. L. Deck, 1988: Fluxes of particles and constituents to the eastern United States continental slope and rise: SEEP I. *Contin. Shelf Res.*, **8**, 855–904.

Butman, B., and R. C. Beardsley, 1987: Long-term observations on the southern flank of Georges Bank. Part I: A description of the seasonal cycle of currents, temperature, stratification and wind stress. *J. Phys. Oceanogr.*, **17**, 367–384.

Chapman, D. C., 1986: A simple model of the formation and maintenance of the shelf-slope front in the Middle Atlantic Bight. *J. Phys. Oceanogr.*, **16**, 1273–1279.

——, J. A. Barth, R. C. Beardsley and R. G. Fairbanks, 1986: On the continuity of mean flow between the Scotian Shelf and the Middle Atlantic Bight. *J. Phys. Oceanogr.*, **16**, 758–772.

Churchill, J. H., P. E. Biscaye and F. Aikman III, 1988: The character and motion of suspended particulate matter over the shelf edge and upper slope off Cape Cod. *Contin. Shelf Res.*, **8**, 789–809.

Coachman, L. K., 1986: Circulation, water masses, and fluxes on the southeastern Bering Sea shelf. *Contin. Shelf Res.*, **5**, 23–108.

Csanady, G. T., 1978: The arrested topographic wave. *J. Phys. Oceanogr.*, **8**, 47–62.

——, 1984: The influence of wind stress and river runoff on a shelf-sea front. *J. Phys. Oceanogr.*, **14**, 1383–1392.

Fiadeiro, M. E., and G. Veronis, 1977: On weighted-mean schemes for the finite-difference approximation to the advection-diffusion equation. *Tellus*, **29**, 512–522.

Garrett, C., and E. Horne, 1978: Frontal circulation due to cabbeling and double diffusion. *J. Geophys. Res.*, **83**, 4651–4656.

——, J. Middleton, M. Hazen and F. Majaess, 1985: Tidal currents and eddy statistics from iceberg trajectories off Labrador. *Science*, **227**, 1333–1335.

Garvine, R. W., K.-C. Wong and G. Gawarkiewicz, 1989: Quantitative properties of shelfbreak eddies. *J. Geophys. Res.*, **94**, 14 475–14 483.

Haidvogel, D., J. Wilkin and R. Young, 1991: A semi-spectral primitive equation ocean circulation model using vertical sigma and orthogonal curvilinear horizontal coordinates. *J. Comput. Physics*, in press.

Hedstrom, K., 1990: User's manual for a semispectral primitive equation regional ocean-circulation model version 3.0 B. Tech. Rep. SR-1, Institute for Naval Oceanography, 82 pp.

Hsueh, Y., and B. Cushman-Roisin, 1983: On the formation of surface to bottom fronts over steep topography. *J. Geophys. Res.*, **88**, 743–750.

Lyne, V. D., and G. T. Csanady, 1984: A compilation and description of hydrographic transects of the Mid-Atlantic Bight shelf-break front. Woods Hole Oceanographic Institution Tech. Rep. WHOI-84-19, 290 pp.

Orlanski, I., 1976: A simple boundary condition for unbounded hyperbolic flows. *J. Comput. Phys.*, **21**, 251–269.

Ou, H. W., 1983: Some two-layer models of the shelf-slope front: Geostrophic adjustment and its maintenance. *J. Phys. Oceanogr.*, **13**, 1798–1808.

——, 1984: Geostrophic adjustment: A mechanism for frontogenesis. *J. Phys. Oceanogr.*, **14**, 994–1000.

Pedlosky, J., 1979. *Geophysical Fluid Dynamics*, first edition. Springer-Verlag, 710 pp.

Pingree, R. D., G. T. Mardell, P. M. Holligan, D. K. Griffiths and J. Smithers, 1982: Celtic Sea and Armorican current structure and the vertical distributions of temperature and chlorophyll. *Contin. Shelf Res.*, **1**, 99–116.

Walsh, J. J., G. T. Rowe, R. L. Iverson and C. P. McRoy, 1981: Biological export of shelf carbon as a neglected sink of the global CO_2 cycle. *Nature*, **291**, 196–201.

——, P. E. Biscaye and G. T. Csanady, 1988: The 1983–1984 Shelf Edge Exchange Processes (SEEP)-I Experiment: Hypotheses and highlights. *Contin. Shelf Res.*, **8**, 435–456.

Wang, D.-P., 1982: Effects of continental slope on the mean shelf circulation. *J. Phys. Oceanogr.*, **12**, 1524–1526.

——, 1984: Mutual intrusion of a gravity current and density front formation. *J. Phys. Oceanogr.*, **14**, 1191–1199.